AIAA JOURNAL
Vol. 38, No. 2, February 2000

Absorption of Sound near Abrupt Area Expansions

I. D. J. Dupère* and A. P. Dowling†
Cambridge University, Cambridge, England CB2 1PZ, United Kingdom

Sound incident onto an abrupt area expansion in a channel is investigated both numerically and analytically. In the presence of a mean flow, the incident sound leads to unsteady vortex shedding from the lip of the expansion, thereby converting acoustic into vortical energy. We use an acoustic analogy and Green's functions to determine the sound reflected and transmitted across the area change. We compare predictions obtained from three different Green's functions with source terms derived either using a simple analytical model or from a numerical calculation. The compact Green's function, with zero normal derivative on the duct walls, gives the best results for a low-Mach-number flow. This Green's function contains a singularity at the lip of the expansion (and hence acoustic sources near the lip have the greatest effect). This means that our estimate of the overall vorticity field can be relatively crude, when using the compact Green's function, provided it is accurate near the lip. Therefore, although predictions for the radiated sound field made using all three Green's functions are formally correct, the solution made using the compact Green's function is less susceptible to errors in the source terms and gives more accurate results. In addition, we find that there is a Strouhal number at which sound absorption is maximized and that this absorption can be enhanced by multiple reflections from the duct ends. Our predictions are compared with an experiment.

I. Introduction

PIPEWORK systems of the type used in car and gas turbine exhausts, or to transport water or natural gas, frequently involve the propagation of acoustic waves and a mean flow. In many pipework systems there are regions where the flow separates, such as at an abrupt area change, an orifice plate, or at a side branch.[1–8] In these regions there may be coupling and energy exchange between acoustic waves and vortical disturbances, leading to absorption. Indeed, Borth[9] found, as long ago as 1916, that pressure oscillations in a duct could be damped using a throttle. Today, devices involving vortex shedding, such as orifice plates and perforated screens, are often used to absorb sound (see Ref. 2 for a list of devices). In the absence of a mean flow, the vortex shedding process is nonlinear, and large levels of excitation are required before significant absorption is observed.[10–13] When there is a mean flow, however, the shed vorticity is swept downstream, and the strength of the vortex sheet formed depends linearly on the amplitude of the incident sound waves. Under these circumstances, significant absorption is observed even for modest levels of excitation.[14–16]

In this paper we investigate this energy exchange for a simple two-dimensional flow past a backward-facing step with flow using an acoustic analogy from Howe[14] to relate the acoustic sources to the shed vorticity. Initially, we consider two semi-infinite channels of height h and $H (h < H)$ joined at $y_1 = 0$. There is a mean flow along the channel that separates at the rearward-facing step. We determine the transmission and reflection of an incident sound wave at the step including the effects of the mean flow. This problem is investigated both numerically and analytically.

Vortex-sound interaction is of fundamental interest in aeroacoustics, and this simple geometry enables us to investigate solution techniques and compare theoretical results with experiment. To relate the sources from the acoustic analogy to the sound that radiates away from the junction, we must introduce a suitable Green's function for the pipework system. The choice of Green's function is crucial to the solution, and three different Green's functions are calculated. Two of these are derived from expansions in terms of modes of straight-walled semi-infinite pipes, whereas the remaining one, the compact Green's function, satisfies boundary conditions of zero normal velocity on all rigid surfaces. The compact Green's function has a singularity at the lip of the expansion, and so sources near the lip have a greater effect on the sound that radiates to the far field than those farther away. This is important because it implies that, when using the compact Green's function, our prediction for the vorticity field, whether from an analytical model or from a numerical calculation, can be relatively crude provided that the vorticity near the lip is accurately predicted. As a result, we postulate that the most accurate results will be obtained using the compact Green's function. The calculation of these Green's functions is discussed in Sec. III.

The vorticity field is obtained in two ways: using an analytical model (Sec. IV.A) and using computational fluid dynamics (CFD; Sec. IV.B) with comparison between the two. The analytical model that we use for the vorticity is that of Howe[17] and assumes that the strength of the shed vorticity is unchanged as it convects downstream and it forms an infinitely thin vortex sheet whose strength is determined by the application of the Kutta condition. In contrast, our numerical calculation uses a crude zero-equation turbulence model and the strength of the vorticity diffuses and decays as it convects downstream as a result of numerical diffusion. Despite the apparent differences between the two models, we show in Sec. V that the radiated sound fields, which they predict, are very similar because of the importance of the region near the lip, provided the compact Green's function is used in the calculation of the far-field sound.

Our initial calculations are for two semi-infinite pipes, but predictions for finite length pipes are obtained in Sec. VI by the introduction of a reflection coefficient at the pipe exit. Solutions for finite length channels are easily derived from the infinite channel solutions, which is important because it implies that, for a particular expansion ratio and Mach number, the infinite channel solution is all that is required; the solution for any length channel can then be deduced from this.

We justify our results by comparison with an experiment and discuss the implication for the absorption of incident sound waves. In particular, we find, for infinite channels, there is an optimum Strouhal number at which maximum absorption is achieved. When wave reflection from the ends of finite length pipes is included, channel resonances can amplify this absorption.

II. Acoustic Analogy

Consider the channel system illustrated in Fig. 1. Two semi-infinite, two-dimensional channels, of heights h and H, respectively, are joined at $y_1 = 0$. A high-Reynolds-number, low-Mach-number flow passes from the smaller (originating at $y_1 = -\infty$) to the larger channel (where it is exhausted at $y_1 = +\infty$). A low-frequency

Presented as Paper 98-2303 at the AIAA/CEAS 4th Aeroacoustics Conference, Toulouse, France, 2–4 June 1998; received 15 September 1998; revision received 6 July 1999; accepted for publication 7 July 1999.

*Research Associate, Engineering Department.
†Professor of Mechanical Engineering, Engineering Department.

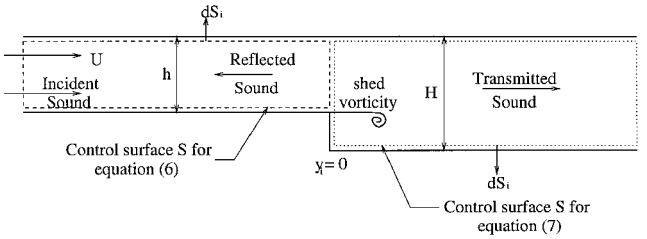

Fig. 1 Two-dimensional flow over a backward-facing step.

incident plane sound wave, of angular frequency ω, propagates from left to right toward the expansion, where it is partly reflected and partly transmitted into the larger channel. We wish to calculate the reflection and transmission coefficients, and hence the absorption coefficient Δ, across the expansion when the effects of the mean flow are included.

The sound generated from a region of isentropic, low-Mach-number, inviscid flow can be determined by an acoustic analogy.[14, 18] Howe[17] showed that the stagnation enthalpy B is a convenient dependent variable: $B = c_p T + \frac{1}{2}|\boldsymbol{v}|^2$, where T is the temperature, ρ is the density, and $\boldsymbol{v}$ is the fluid velocity. In a unidirectional acoustic wave B' the fluctuating part of B is related to the pressure perturbation by $B' = p'(1 + M)$, where M is the mean flow Mach number in the direction of propagation. In terms of B, the acoustic analogy takes the form

$$\frac{1}{c^2}\left(\frac{\partial}{\partial \tau} + U_i \frac{\partial}{\partial y_i}\right)^2 B - \frac{\partial^2 B}{\partial y_i^2} = \frac{\partial}{\partial y_i}(\omega \wedge \boldsymbol{v})_i - \frac{1}{c^2}\frac{\partial v_i}{\partial \tau}(\omega \wedge \boldsymbol{v})_i \quad (1)$$

where c is the speed of sound, τ is the time, ω is the vorticity vector, and y_i is the spatial position in the i direction. In this equation $\boldsymbol{U}$ is a hypothetical steady potential flow that is equal to the mean flow as $y_1 \to \pm\infty$ (Ref. 18). Terms of the order of the square of the Mach number have been neglected in comparison with unity in the derivation of Eq. (1).

The transmission coefficient is obtained from the solution to Eq. (1) for an observer positioned far downstream of the area change (i.e., $y_1 \to +\infty$), whereas the reflection coefficient is obtained by considering an observer positioned far upstream (i.e., for $y_1 \to -\infty$).

Physically, the mean flow separates at the abrupt area expansion ($y_1 = 0$) to form a jet in the larger channel. In addition the incident sound waves cause unsteady vorticity to be shed at the lip of the expansion, which is subsequently convected downstream by the mean flow. It is this convecting unsteady vorticity that provides the main source term. Applying a Green's function $G(\boldsymbol{y}, \tau \mid \boldsymbol{x}, t)$, in the usual way, enables us to write a formal solution to Eq. (1):

$$H_v(\boldsymbol{x})B(\boldsymbol{x}, t) = \int_\tau \int_S \left[\frac{\partial G}{\partial \tau}\left(2\frac{U_i}{c^2}B + v_i\right) - B\frac{\partial G}{\partial y_i}\right] \mathrm{d}S_i \, \mathrm{d}\tau + \int_\tau \int_V \left(\frac{v_i}{c^2}\frac{\partial G}{\partial \tau} - \frac{\partial G}{\partial y_i}\right)(\omega \wedge \boldsymbol{v})_i \, \mathrm{d}^3 y \, \mathrm{d}\tau \quad (2)$$

where S is a fixed control surface bounding the volume V, $\mathrm{d}S_i$ is the i component of the outward normal, v_i is the i component of the total flow velocity, and $H_v(\boldsymbol{x})$ is unity for $\boldsymbol{x}$ in V and zero otherwise.

Notice that we integrate over the inner flowfield $\boldsymbol{y}$ to obtain the sound radiated to the far field at $\boldsymbol{x}$. The sound radiated to a position $(\boldsymbol{x}, t)$ depends upon the volume integral of the shed vorticity impulse and upon a surface integral involving B and v_i. The representation in Eq. (2) is formally exact for any Green's function that satisfies the convected wave equation:

$$\frac{1}{c^2}\left(\frac{\partial}{\partial \tau} + U_i \frac{\partial}{\partial y_i}\right)^2 G - \frac{\partial^2 G}{\partial y_i^2} = \delta(\boldsymbol{x} - \boldsymbol{y})\delta(t - \tau) \quad \text{in} \quad V \quad (3)$$

However, by the choice of appropriate boundary conditions for the Green's function, we can eliminate some (or all) of the surface terms in Eq. (2). $G(\boldsymbol{x}, \boldsymbol{y}, t, \tau)$ is a reciprocal Green's function, i.e., it is the response at $\boldsymbol{y}$ caused by a sink at the observer position $\boldsymbol{x}$. The appropriate far-field boundary condition is therefore

$$\text{inward wave behavior in the variables } \boldsymbol{y} \text{ and } \tau \text{ as } y_1 \to \pm\infty \quad (4)$$

This ensures outward propagating waves in $(\boldsymbol{x}, t)$ and eliminates any contributions from outgoing acoustic waves in Eq. (2). In addition, all of the Green's functions we consider have

$$\frac{\partial G}{\partial y_2} = 0 \text{ on the channel side walls} \quad (5)$$

This eliminates surface contributions from the side walls. Two of the Green's functions we use are based upon a straight-walled semi-infinite duct geometry. For them it is appropriate to apply the representation in Eq. (2) separately in the two regions $y_1 > 0$ and $y_1 < 0$, using the control surfaces sketched in Fig. 1. This leads to

$$H(x_1)B(\boldsymbol{x}, t) = -\int_{-\infty}^{\infty}\int_{-\infty}^{\infty}\int_0^H \left[v_1\frac{\partial G}{\partial \tau} - B\left(\frac{\partial G}{\partial y_1} - 2\frac{U_1}{c^2}\frac{\partial G}{\partial \tau}\right)\right]_{y_1 = 0^+} \mathrm{d}y_2 \, \mathrm{d}y_3 \, \mathrm{d}\tau + \int_\tau \int_V \left[\left(\frac{v_i}{c^2}\frac{\partial G}{\partial \tau} - \frac{\partial G}{\partial y_i}\right)(\omega \wedge \boldsymbol{v})_i\right] \mathrm{d}^3 y \, \mathrm{d}\tau \quad (6)$$

$$H(-x_1)B(\boldsymbol{x}, t) = \int_{-\infty}^{\infty}\int_{-\infty}^{\infty}\int_0^h \left[v_1\frac{\partial G}{\partial \tau} - B\left(\frac{\partial G}{\partial y_1} - 2\frac{U_1}{c^2}\frac{\partial G}{\partial \tau}\right)\right]_{y_1 = 0^-} \mathrm{d}y_2 \, \mathrm{d}y_3 \, \mathrm{d}\tau - \int_{-\infty}^{\infty}\int_{-\infty}^{\infty}\int_0^h \left[2(1 + M_1)B_{\text{in}}\frac{\partial G}{\partial y_1}\right]_{y_1 = -\infty} \mathrm{d}y_2 \, \mathrm{d}y_3 \, \mathrm{d}\tau \quad (7)$$

$H(x)$ is the Heaviside function. B_{in} is the fluctuating stagnation enthalpy at inlet caused by an incident sound wave propagating from left to right from $y_1 = -\infty$, where the mean flow Mach number is M_1. We have used the fact that the vorticity ω is only nonzero downstream of the step. One of the Green's functions we use, G_v, satisfies

$$\frac{\partial G_v}{\partial y_1} = 2\frac{U_1}{c^2}\frac{\partial G_v}{\partial \tau} \quad \text{on} \quad y_1 = 0 \quad (8)$$

This boundary condition eliminates the terms involving B at the junction $y_1 = 0$. The interaction between the ducts is then described in terms of the axial velocity v_1 at their junction. For the second Green's function G_B, we choose

$$G_B = 0 \quad \text{on} \quad y_1 = 0 \quad (9)$$

With this boundary condition the duct interaction is described via the values of the stagnation enthalpy B at the junction. The third Green's function we use G_c is a compact Green's function, which satisfies $\partial G_c/\partial n = 0$ on all of the rigid walls. Then $\partial G_c/\partial y_1 = 0$ on $y_1 = 0$, $h - H \le y_2 \le 0$ and G_c and its derivatives are continuous across $y_1 = 0$, $0 \le y_2 \le h$. The surface integrals at $y_1 = 0$ in Eqs. (6) and (7) are then equal and opposite, and after adding these two equations we obtain

$$B(\boldsymbol{x}, t) = \int_\tau \int_V \left(\frac{v_i}{c^2}\frac{\partial G_c}{\partial \tau} - \frac{\partial G_c}{\partial y_i}\right)(\omega \wedge \boldsymbol{v})_i \, \mathrm{d}^3\boldsymbol{y} \, \mathrm{d}\tau - \int_{-\infty}^{\infty}\int_{-\infty}^{\infty}\left[2(1 + M_1)B_{\text{in}}\frac{\partial G_c}{\partial y_1}\right] \mathrm{d}y_2 \, \mathrm{d}y_3 \, \mathrm{d}\tau \quad (10)$$

To complete our solution, we need to determine the Green's functions (which we can do analytically a priori) and the vortical flowfield (which we can obtain either analytically or numerically). We start by calculating the Green's functions.

III. Calculation of the Green's Functions

Because the problem is essentially a two-dimensional one, the source terms are independent of the 3 direction. The integration over y_3 in Eq. (10) can be performed by using the two-dimensional Green's functions, which describe the effect of a line source. The Green's functions discussed next satisfy the two-dimensional wave equation.

A. Green's Functions for Straight-Walled Pipes

G_v and G_B are calculated by separating G into two: one function valid for $y_1 < 0$ and one for $y_1 > 0$. In these cases we allow $\boldsymbol{U}$ to be discontinuous at $y_1 = 0$ and write

$$\begin{aligned} \boldsymbol{U} &= (U_1, 0, 0), \qquad y_1 > 0 \\ &= (U_2, 0, 0), \qquad y_1 < 0 \end{aligned} \tag{11}$$

where $U_2 = U_1 h/H$. The boundary conditions at $y_1 = 0$ are written in general form so that we can calculate G_v and G_B simultaneously:

$$\frac{\partial G}{\partial y_1} = \alpha G + \beta \frac{\partial G}{\partial \tau} \qquad \text{on} \qquad y_1 = 0 \tag{12}$$

First we calculate the case for $x_1, y_1 > 0$. Condition (5) is satisfied by expanding G as a Fourier series in y_2, and the behavior in time is expressed by writing G as a Fourier transform. Thus we have

$$G(\boldsymbol{y}, \tau \mid \boldsymbol{x}, t) = \sum_{n=0}^{\infty} \int \frac{1}{2\pi} a_n(y_1, \omega \mid \boldsymbol{x}, t) \cos\left(\frac{n\pi y_2}{H}\right) \exp(i\omega\tau)\, \mathrm{d}\omega \tag{13}$$

Substituting Eq. (13) into Eq. (3) and solving subject to conditions (4) and (12) (Ref. 18):

$$\begin{aligned} a_m = \frac{i S_m \cos(m\pi x_2/H)}{H\delta_m} &\left\{ \exp(i\delta_m |y_1 - x_1|) \right. \\ &\left. + \frac{\delta_m - kM_2 + \omega\beta - i\alpha}{\delta_m + kM_2 - \omega\beta + i\alpha} \exp[i\delta_m (y_1 + x_1)] \right\} \\ &\times \exp[-i\omega t + ikM_2(y_1 - x_1)] \end{aligned} \tag{14}$$

where $k = \omega/c$, $M_2 = U_2/c$, and $S_0 = \frac{1}{2}$, $S_m = 1$, $m \geq 1$, and $\delta_m = \sqrt{[k^2 - (m\pi/H)^2]}$. When δ_m is complex, the root is to be chosen to have positive imaginary part. Equation (14) combined with Eq. (13) define the Green's function G for $y_1, x_1 > 0$ for the general boundary condition at $y_1 = 0$ given by Eq. (12). Similarly for $y_1, x_1 < 0$,

$$G(\boldsymbol{y}, \tau \mid \boldsymbol{x}, t) = \sum_{m=0}^{\infty} \int b_m(y_1, \omega \mid \boldsymbol{x}, t) \cos\left(\frac{m\pi y_2}{h}\right) \exp(i\omega\tau)\, \mathrm{d}\omega \tag{15}$$

$$\begin{aligned} b_m = \frac{i S_m \cos(m\pi x_2/h)}{h\gamma_m} &\left\{ \exp(i\gamma_m |y_1 - x_1|) \right. \\ &\left. + \frac{\gamma_m + kM_1 - \omega\beta + i\alpha}{\gamma_m - kM_1 + \omega\beta - i\alpha} \exp[-i\gamma_m (y_1 + x_1)] \right\} \\ &\times \exp[-i\omega t + ikM_1(y_1 + x_1)] \end{aligned} \tag{16}$$

where $\gamma_m = \sqrt{[k^2 - (m\pi/h)^2]}$ and the root is chosen to give a positive imaginary part if γ_m is complex. Equation (16) combined with Eq. (15) define the Green's function G for $y_1 < 0$ for the general boundary condition at $y_1 = 0$ given by Eq. (12). For large $|x_1|$ we can derive a simpler form of the Green's function for use with low-frequency sources. For frequencies at which $kH < \pi$, all modes with $m \geq 1$ decay as $|x_1| \to \infty$. Then the Green's function just consists of plane wave terms, $m = 0$. For the velocity and enthalpy Green's functions that satisfy the boundary conditions in Eqs. (8) and (9), further simplification is possible.

The boundary conditions for the velocity Green's function G_v are given in Eq. (8) and are equivalent to the general form in Eq. (12) with

$$\alpha = 0, \qquad \beta = 2M_1/c \tag{17}$$

whereas those for G_B in Eq. (9) can be written as

$$\alpha = 0, \qquad \beta = \infty \tag{18}$$

Applying these two forms in turn to the plane wave terms in Eqs. (13) and (15) leads to a simple approximate form of the Green's function for use with low-frequency sources. In particular,

$$\begin{bmatrix} \nabla G_v \\ \nabla G_B \end{bmatrix} = \left\{ \frac{\delta[t - \tau - (x_1 - y_1)/c(1 + M_2)]}{2H(1 + M_2)} \right. \\ \left. \mp \frac{\delta[t - \tau - x_1/c(1 + M_2) - y_1/c(1 - M_2)]}{2H(1 - M_2)} \right\}, \qquad x_1 \gg y_1 \geq 0 \tag{19}$$

$$\begin{bmatrix} \nabla G_v \\ \nabla G_B \end{bmatrix} = \left\{ \frac{\delta[t - \tau + (x_1 - y_1)/c(1 - M_1)]}{2h(1 - M_1)} \right. \\ \left. \mp \frac{\delta[t - \tau + x_1/c(1 - M_1) + y_1/c(1 + M_1)]}{2h(1 + M_1)} \right\}, \qquad x_1 \ll y_1 \leq 0 \tag{20}$$

$$\begin{bmatrix} \frac{1}{c}\frac{\partial G_v}{\partial \tau}\Big|_{y_1 = 0^+} \\ \frac{\partial G_B}{\partial y_1}\Big|_{y_1 = 0^+} \end{bmatrix} = \frac{1}{H}\delta\left[t - \tau - \frac{x_1}{c(1 + M_1)}\right], \qquad x_1 \gg 0 \tag{21}$$

$$\begin{bmatrix} \frac{1}{c}\frac{\partial G_v}{\partial \tau}\Big|_{y_1 = 0^-} \\ \frac{\partial G_B}{\partial y_1}\Big|_{y_1 = 0^-} \end{bmatrix} = \mp \frac{\delta[t - \tau + x_1/c(1 - M_1)]}{h}, \qquad x_1 \ll 0 \tag{22}$$

where the upper signs of the right-hand side are for G_v and the lower for G_B. The downstream radiated sound field can now be found by using the Green's function defined by Eqs. (19) and (21) into Eq. (6), whereas the upstream radiated sound field can be calculated by substituting G_v from Eqs. (20) and (22) into Eq. (7).

B. Compact Green's Function

An exact Green's function $G(\boldsymbol{x}, t \mid \boldsymbol{y}, \tau)$ satisfies

$$\frac{1}{c^2}\left(\frac{\partial}{\partial \tau} + U_i \frac{\partial}{\partial y_i}\right)^2 G - \frac{\partial^2 G}{\partial y_i^2} = \delta(x_1 - y_1)\delta(x_2 - y_2)\delta(t - \tau) \tag{23}$$

with the boundary conditions

$$\text{inward behavior in } (\boldsymbol{y}, \tau) \text{ at infinity} \tag{24}$$

$$\frac{\partial G}{\partial n} = 0 \text{ on the channel walls} \tag{25}$$

$\boldsymbol{U}(\boldsymbol{y})$ is now continuous and describes a hypothetical steady potential flow through the expansion.

In the Appendix we find an approximation to the exact Green's function for use with low-frequency sources (Fig. 2). It is derived making use of the velocity potential $\Phi(\boldsymbol{y})$ for incompressible flow

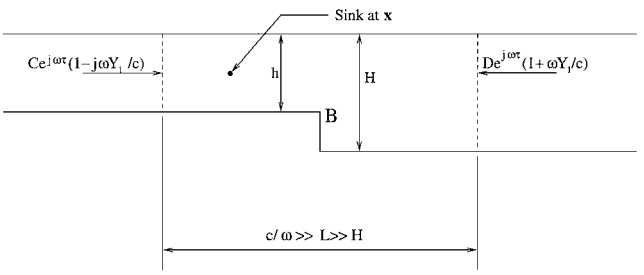

Fig. 2 Green's function for x in the inner flowfield.

past the rearward-facing step and an approximation appropriate for low-frequency waves.[25–27] For $\boldsymbol{x}$ in the far field and $\boldsymbol{y}$ near the step, we show that the Fourier transform of $G_c(\boldsymbol{x}, t \mid \boldsymbol{y}, \tau)$ is given by

$$\hat{G}_c \exp(i\omega\tau) = -\frac{\exp\{i\omega[\tau - t - x_1/c(1 - M_1)]\}}{ik(H + h)}[1 + ik\Phi(\boldsymbol{y})] \qquad x_1 \ll 0 \quad (26)$$

$$= -\frac{\exp\{i\omega[\tau - t + x_1/c(1 + M_2)]\}}{ik(H + h)} \times \left[1 - ik\frac{h}{H}\Phi(\boldsymbol{y})\right] \qquad 0 \ll x_1 \quad (27)$$

Φ can be calculated using a Schwarz–Christoffel transformation,[19] which maps $z = y_1 + iy_2$ into a transformed variable ζ. With $\boldsymbol{x}$ in the far field, potential flow through the channel is determined by a point source at $\zeta = 0$ and so $\Phi \propto \ln\zeta$. The solution that satisfies $\Phi \to Y_1$ as $Y_1 \to \infty$ is

$$\Phi = (H/\pi)\ln\zeta \quad (28)$$

where ζ is conveniently expressed in terms of a new variable s:

$$\zeta = \frac{s^2 - (H/h)^2}{s^2 - 1} \quad (29)$$

and s is defined through the relationship

$$z = \frac{H}{\pi}\left[\ln\left(\frac{1 + s}{1 - s}\right) - \frac{h}{H}\ln\left(\frac{H/h + s}{H/h - s}\right)\right] - i(H - h) \quad (30)$$

Alternative forms for G_c appropriate for use when $\boldsymbol{x}$ and $\boldsymbol{y}$ are both in the far field and when they are both in the near field are given in the Appendix.

IV. Calculation of the Source Field

Equation (2) relates the far-field sound to the vorticity impulse [characterized by $\nabla\cdot(\omega\wedge\boldsymbol{v})$]. The vorticity impulse is obtained by two different methods: using an analytical model (Sec. IV.A) and from a CFD calculation of the flowfield (Sec. IV.B). Because we are concerned with the transmission of an incident sound wave, we restrict our attention to the vortex shedding caused by the incident sound.

A. Analytical Description of the Source Field

Conformal transformation shows that, in inviscid flow, sound waves incident from upstream or from downstream of the sudden area expansion give rise to a singularity in velocity of the form $(|\boldsymbol{y}|/h)^{-1/3}$ near the lip of the expansion (for an origin at the lip). In reality, however, viscous effects lead to the shedding of unsteady vorticity from the lip, thereby suppressing this singularity. This unsteady vorticity subsequently convects downstream with a velocity of approximately $0.6\bar{u}$. We follow Howe's approach[14] and approximate this unsteady vorticity distribution by an infinitesimally thin vortex sheet convecting away at a velocity $\bar{u}_c$. Such a vortex sheet also leads to a singularity in the velocity of the order $(|\boldsymbol{y}|/h)^{-1/3}$. The strength of the vorticity is then determined by applying the unsteady Kutta condition so that both singularities exactly cancel each other at the lip.

The vorticity source term $\nabla\cdot(\omega\wedge\boldsymbol{v})$ is approximated in a way suggested by Howe.[14] For low-amplitude sound waves the the unsteady flow can be linearized as follows:

$$\nabla\cdot(\omega\wedge\boldsymbol{v}) = \nabla\cdot(\bar{\omega}\wedge\bar{\boldsymbol{u}}) + \nabla\cdot(\omega'\wedge\bar{\boldsymbol{u}}) + \nabla\cdot(\bar{\omega}\wedge\boldsymbol{u}') \quad (31)$$

Howe argues that for a mean shear layer, which is thick in comparison with $(2\nu/\omega)^{1/2}$, the thickness of the acoustic shear layer,[20] the third term on the right-hand side of Eq. (31) is small in comparison with the second and may be safely neglected. This assumption is confirmed by the numerical calculation in Sec. IV.B, where the third term is found to be, at most 6% of the second term. Following Howe,[14] the unsteady part of the shed vorticity is modeled by assuming that it forms an infinitesimally thin vortex sheet, which simply convects downstream at a velocity $\bar{u}_c$ as just described:

$$\omega' = H(y_1)\delta(y_2)\sigma\exp[-i\omega(t - y_1/\bar{u}_c)]\boldsymbol{k} \quad (32)$$

where σ is the strength per unit length of the vortex sheet, $H(y_1)$ is the Heaviside function, $\delta(y_2)$ is the Dirac function, and $\boldsymbol{k}$ is the unit vector in the 3 direction. The vorticity strength σ is to be determined by the imposition of the unsteady Kutta condition at the lip of the expansion.

To apply the unsteady Kutta condition, we need to determine the unsteady velocities that would be induced by the potential flow caused by an incident plane sound wave propagating toward the expansion from $y_1 = -\infty$. We then add the effect of the convected vorticity and choose σ so as to make the total velocity field finite. We can calculate the unsteady velocity from Crocco's form of the momentum equation:

$$-\frac{\partial v_i'}{\partial t} = -i\omega v_i' = \frac{\partial B}{\partial x_i} + (\omega\wedge\boldsymbol{v})_i \quad (33)$$

in inviscid, isentropic flow. The unsteady velocity and stagnation enthalpy are then decomposed into terms directly caused by the incident sound wave and those caused by the shed vorticity:

$$v_i' = v_{i,\mathrm{irr}}' + v_{i,\mathrm{vort}} \quad (34)$$

$$B = B_{\mathrm{irr}} + B_{\mathrm{vort}} \quad (35)$$

where

$$-i\omega v_{i,\mathrm{irr}}' = \frac{\partial B_{\mathrm{irr}}}{\partial x_i} \quad (36)$$

$$-i\omega v_{i,\mathrm{vort}} = \frac{\partial B_{\mathrm{vort}}}{\partial x_i} + (\omega\wedge\boldsymbol{v})_i(\boldsymbol{x}) \quad (37)$$

$\nabla B_{\mathrm{irr}}(\boldsymbol{x} = 0)$ can be determined by substituting for G_c from Eq. (A23) into Eq. (10) and differentiating in the absence of any source terms, i.e.,

$$\frac{\partial B_{\mathrm{irr}}(0,t)}{\partial x_i} = -\frac{\partial}{\partial x_i}\int_\tau\int_S\left\{\left[2(1 + M_1)B_{\mathrm{in}}\frac{\partial G_c}{\partial y_1}\right]_{y_1 = -\infty}\mathrm{d}S_i\,\mathrm{d}\tau\right\} \quad (38)$$

Because $B_{\mathrm{in}} = B_0\exp\{-i[\omega t - ky_1/(1 + M_1)]\}$, this leads to

$$v_{i,\mathrm{irr}}'(0,t) = -\int_\tau\int_S\frac{2B_{\mathrm{in}}}{c}\frac{\partial G_c}{\partial x_i}(0, t \mid \boldsymbol{y}, \tau)\,\mathrm{d}S_i\,\mathrm{d}\tau \quad (39)$$

$(\partial G_c/\partial x_i)(0, t \mid \boldsymbol{y}, \tau)$ is obtained by differentiating Eq. (A23) to give

$$\frac{\partial\hat{G}_c}{\partial x_i}(0, t \mid \boldsymbol{y}, \tau)\exp(-i\omega\tau') = \frac{-\exp[i\omega(\tau' - t')]}{H + h}\left[\frac{\partial\Phi(0)}{\partial X_i} - \frac{1}{c}\frac{\partial\bar{\phi}(0)}{\partial X_i}\right]\exp(-ikY_1) = \frac{-\exp[i\omega(\tau' - t')]}{H + h}(1 + M_2)\boldsymbol{S}(\boldsymbol{x} = 0)\exp(-ikY_1) \quad (40)$$

because $\bar{\phi}(\boldsymbol{X}) = U_2\Phi(\boldsymbol{X})$. $\boldsymbol{S}(\boldsymbol{x} = 0) = \Re(s) - \boldsymbol{j}\Im(s)$, where $\boldsymbol{j}$ is a unit vector in the two direction and s is related to z through Eq. (30). $\boldsymbol{S}$ has a singularity of the form $|z|^{-1/3}$ near $\boldsymbol{x} = 0$. Rewriting in $(\boldsymbol{x}, \boldsymbol{y}, t, \tau)$, we have

$$\frac{\partial\hat{G}_c}{\partial x_i}(0, t \mid \boldsymbol{y}, \tau)\exp(-i\omega t) = \frac{-\exp\{i\omega[\tau - t - y_1/c(1 + M_1)]\}}{H + h} \times (1 + M_2)\boldsymbol{S}(\boldsymbol{x} = 0) \quad (41)$$

$$v_{i,\mathrm{irr}}'(0,t) = \frac{2h(1 + M_2)}{c(H + h)}B_0\exp(-i\omega t)\boldsymbol{S}(\boldsymbol{x} = 0) \quad (42)$$

Similarly, the unsteady velocities induced by the shed vorticity are obtained by differentiating Eq. (A20):

$$-i\omega v_{i,\text{vort}} = -\int_V \int_\tau (\omega \wedge \boldsymbol{v})_i \frac{\partial^2 G_c}{\partial y_i \partial x_i}\,\mathrm{d}V\,\mathrm{d}\tau + (\omega \wedge \boldsymbol{v})(\boldsymbol{x}) \tag{43}$$

$$= -\int_0^\infty \int_\tau \sigma \bar{u}_c \exp\left(\frac{i\omega y_1}{\bar{u}_c}\right)\frac{\partial^2 G_c}{\partial y_2 \partial x_i}\,\mathrm{d}y_1\,\mathrm{d}\tau + \sigma \bar{u}_c \exp\left(\frac{i\omega x_1}{\bar{u}_c}\right)H(x_1)\delta(x_2)$$

$$= -I_1 \sigma \bar{u}_c \boldsymbol{S}(\boldsymbol{x}=0)\exp(-i\omega t) + \sigma \bar{u}_c \exp\left(\frac{i\omega x_1}{\bar{u}_c}\right)H(x_1)\delta(x_2) \tag{44}$$

where

$$I_1 = \int_0^\infty \exp\left(\frac{i\omega y_1}{\bar{u}_c}\right) I_2\,\mathrm{d}y_1 \tag{45}$$

$$\int_\tau I_2 = \left\{\Im\left[\frac{-\pi}{H^2}\frac{\zeta}{(\zeta-1)^2} + ik\left(\frac{h/H}{H+h} - M_2\right)\right]s(y_1,0)\right\}\mathrm{d}\tau$$

For $y_1 \to 0$

$$\Im\left[\frac{\zeta s(y_1,0)}{\zeta - 1}\right] \sim 0, \qquad \Im[s(y_1,0)] \sim O(|y_1|^{-\frac{1}{3}})$$

Hence, although the integrand is singular at $y_1 = 0$, it is integrable and hence I_1 is finite.

As both the incident wave and the shed vorticity have a singularity of the type $\boldsymbol{S}(\boldsymbol{x}=0)$, the unsteady Kutta condition implies

$$\frac{\sigma}{B_0} = \left[\frac{2h(1+M_2)}{c\bar{u}_c(H+h)I_1}\right] \tag{46}$$

The integral in Eq. (46) is evaluated numerically to give the unsteady vorticity strength σ. Checks were made to ensure that the result is independent of both the upper limit of integration used and the step length.

Once we have determined σ, and hence approximated for the source distribution, we can substitute it into the representation Eq. (10) to give the far-field sound:

$$B_{\text{vort}} = \int_0^\infty \frac{\sigma \bar{u}_c \exp(i\omega y_1/\bar{u}_c)}{(H+h)}\Im[s(y_1)]\,\mathrm{d}y_1 \times \exp\left\{-i\omega\left[t + \frac{x_1}{c(1-M_1)}\right]\right\} \tag{47}$$

$$= \frac{h}{H}\int_0^\infty \frac{\sigma \bar{u}_c \exp(i\omega y_1/\bar{u}_c)}{(H+h)}\Im[s(y_1)]\,\mathrm{d}y_1 \times \exp\left\{-i\omega\left[t - \frac{x_1}{c(1+M_1)}\right]\right\} \tag{48}$$

B. Numerical Calculation of the Source Field

In our numerical calculation of the vorticity field, we use a modified version of VISQ3D, an unsteady flow solver developed by Denton.[21] This solves the Reynolds-averaged Navier–Stokes equations using a finite volume, explicit time-stepping approach with nonreflecting boundary conditions at both inlet and exit. Turbulence is handled using a simple zero-equation turbulence model based upon mixing length. The numerical solution was driven by an oncoming plane wave $B_0 \cos \omega[t - x/c(1+M_1)]$, and we use the resulting flow near the lip as the acoustic source terms in the acoustic analogy in Eqs. (6), (7), and (10). For the compact Green's function G_c we need only the vorticity impulse, but for G_v and G_B the flow velocity and stagnation enthalpy at $y_1 = 0$ are also required.

V. Absorption Coefficient

One of the most important physical features of the problem described in this paper is that acoustical energy from the incident sound wave is converted into vortical energy in the mean flow by the shedding of unsteady vorticity from the lip of the expansion. Investigation of this parameter provides a stringent test of the modeling of sound/vortex interaction because without such interaction there is no absorption. Hence it is convenient to express our results as a dependence of the absorption coefficient Δ on the Strouhal number $St_h = \omega h/U_1$. Here the absorption coefficient Δ is defined as the fraction of the incident sound energy that is absorbed:

$$\Delta = \frac{I_{\text{in}}A_1 - I_r A_1 - I_t A_2}{I_{\text{in}}A_1} \tag{49}$$

where I is the intensity and the subscripts in, r, and t denote the incident, reflected, and transmitted sound waves, respectively; and A_1 and A_2 are the areas of the channel upstream and downstream of the expansion, respectively. The magnitudes of the acoustic intensities are given by[22]

$$I_{\text{in}} = \frac{p'^2_{\text{in}}}{\rho c(1+M_1)^2} = B'^2_{\text{in}} \tag{50}$$

$$I_r = \frac{p'^2_r}{\rho c(1-M_1)^2} = B'^2_r \tag{51}$$

$$I_t = \frac{p'^2_t}{\rho c(1+M_2)^2} = B'^2_t \tag{52}$$

where p' is the acoustic pressure and B' is the acoustic stagnation enthalpy.

Thus,

$$\Delta = \frac{p'^2_{\text{in}}(1+M_1)^2}{p'^2_{\text{in}}(1+M_1)^2} - \frac{p'^2_r(1-M_1)^2}{p'^2_{\text{in}}(1+M_1)^2} - \frac{p'^2_t(1+M_2)^2(A_2/A_1)}{p'^2_{\text{in}}(1+M_1)^2} = \frac{B'^2_{\text{in}} - B'^2_r - B'^2_t(A_2/A_1)}{B'^2_{\text{in}}} \tag{53}$$

If the sound field predicted from the analytical calculation is to agree with that from the numerical calculation, then the vorticity source fields should agree in the region that has the greatest effect upon the radiated sound. To check this, we compare the two. Because the model assumes an infinitesimally thin shear layer, however, we first integrate the vorticity impulse across the shear layer (i.e., with respect to y_2). The computational and the analytical results are then compared as a function of y_1 for $y_1 > 0$ in Fig. 3. The agreement is reasonably good near $y_1 = 0$, but worsens downstream where the computational result decays in magnitude while the analytical vortex strength remains unchanged. In reality the vorticity would diffuse downstream of the step, but not as rapidly as predicted by the computational calculation (where numerical diffusion, particularly in the coarse grid downstream of $y_1 = 20$, artificially enhances the decay). The discrepancy between the two profiles, however, has little effect upon the radiated sound field because the vorticity generates very little sound at large distances downstream of the expansion. This is most readily seen by comparing $\int \nabla G_c \cdot (\omega' \wedge \bar{\boldsymbol{u}})\,\mathrm{d}y_2$ downstream to identify the contribution to the acoustic far field. This is shown in Fig. 4.

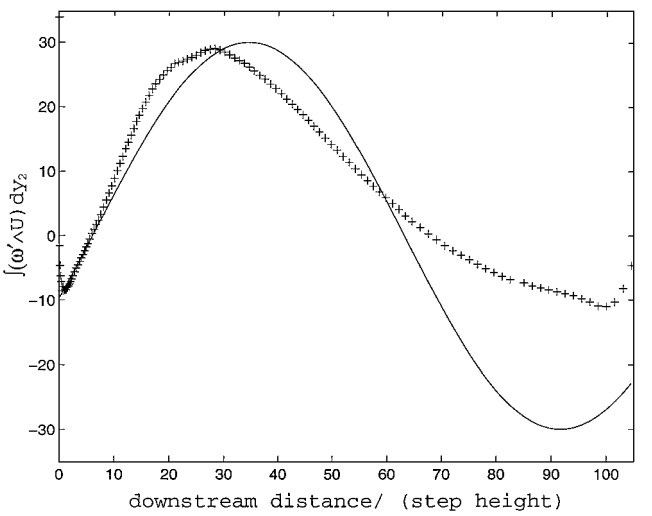

Fig. 3 Comparison between the integrated vorticity field $\int(\omega' \wedge \bar{u})_2\,\mathrm{d}y_2$ from the computation with the integrated vorticity field from the analytical solution for $St_h = \omega h/U_1 = 0.08$, $M_1 = 0.25$, and an expansion ratio of 1.34: ——, analytical, and + , numerical prediction.

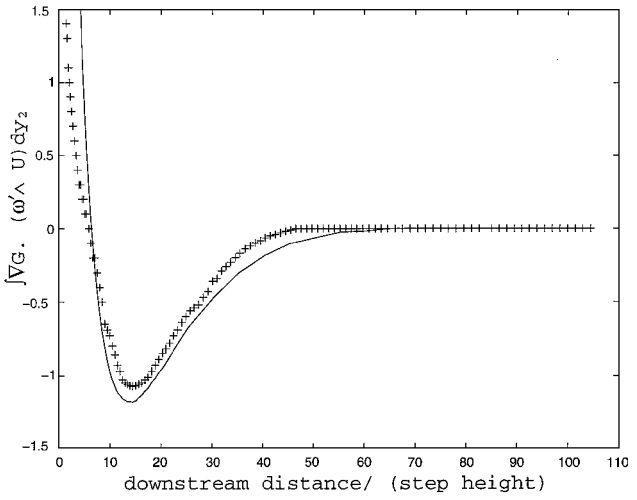

Fig. 4 Comparison between the numerical and analytical calculation for $\int \nabla G \cdot (\omega' \wedge \bar{u})\, dy_2$: ——, analytical, and + , numerical prediction.

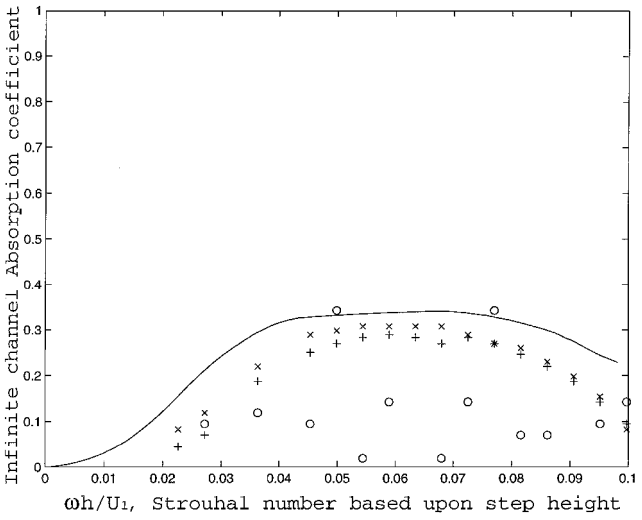

Fig. 5 Comparison of the calculated absorption coefficient made using the three Green's functions and the computational scheme with the analytical prediction: ——, analytical; ×, compact Green's function; + , pressure Green's function G_B; and ○, velocity Green's function G_v.

Near $y_1 = 0$, ∇G_c scales as $y_1^{-1/3}$, which integrates to a negligible term for small y_1. Thus the discrepancy near $y_1 = 0$ has little effect upon the radiated sound field. The gradient of the Green's function decreases rapidly away from the lip, and so it is only in the region just downstream of the step that the vorticity source term has a significant effect. Notice that, after weighting with the compact Green's function, the agreement between the two weighted source terms in Fig. 4 is much better than the agreement seen in Fig. 3. Hence, despite the differences between the two models, the radiated sound fields they predict are very similar. This is the major advantage of the compact Green's function: it is relatively insensitive to inadequacies in the vorticity calculation because of the dominance of the region near the lip in the Green's function.

The calculated results for the absorption coefficient (three computational using three different Green's functions and one analytical) are shown as a function of Strouhal number in Fig. 5 for a Mach number of 0.25 and an expansion ratio of 1.34. All four methods show negligible absorption at very low and very high Strouhal numbers and a maximum absorption over a range of Strouhal numbers between 0.05 and 0.085, based upon step height. When the compact Green's function is used, the agreement with the analytical form is to within 7% near maximum absorption. The error increases to 25% for low Strouhal number, but this is partly because of the larger bandwidth of absorption predicted by the analytical model. When G_B is used, the error near peak absorption is approximately 12%,

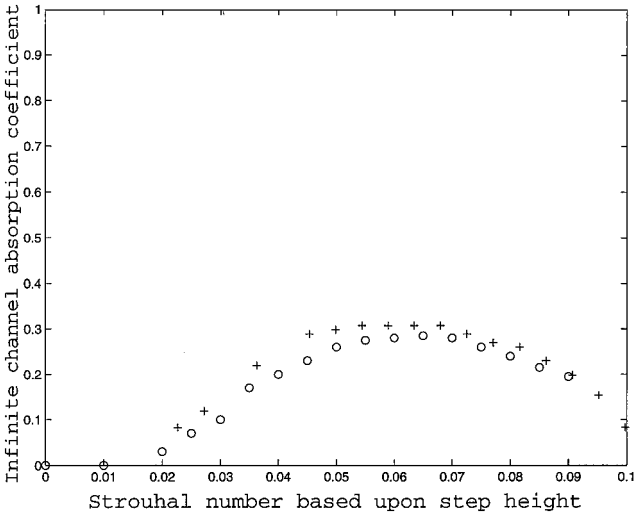

Fig. 6 Predicted absorption for an expansion ratio of 1.34 and a Mach number of 0.25 and varying displacement thickness: + , $\delta^* = 3.5$ mm, and ○, $\delta^* = 4.5$ mm.

increasing to 60% for low Strouhal numbers. Again, this is partly explained by the broader range of Strouhal numbers predicted by the analytical model. When G_v is used, however, the agreement is terrible.

The poor performance of G_v, for which $\partial G/\partial y_1 = 0$ on $y_1 = 0$, is explained as follows. For this case the representation theorems in Eqs. (6) and (7) contain an apparent monopole source term at $y_1 = 0$. This source term is small $\int \partial u_1/\partial t \, dS$ and is nonzero only because of weak compressible effects. This small term arises through the near cancellation on integration of larger point values of $\partial u_1/\partial t$. In the representation theorem this weak source term is multiplied by a large Green's function. If a perfectly accurate description of the flow were available, this would not matter. Here, however, the small errors in $\partial u_1/\partial t$ lead to significant fractional errors in the (nearly zero) integral $\int (\partial u_1/\partial t)\, dS$ and are enhanced by the large Green's function. Thus the solution is very inaccurate.

G_B, on the other hand, leads to a surface integral involving the stagnation enthalpy at $y_1 = 0$, which is predominately dipole, i.e., is multiplied by the small derivative $\partial G_B/\partial y_1$. Because the stagnation enthalpy is significant in this region and it is multiplied by a small term involving the Green's function, this approach is less prone to error than using G_v. Hence the agreement with the analytical expression is much better than for G_v.

G_c requires only the integral of the vorticity field and so is the most accurate of the three Green's functions.

Figures 3 and 4 are for a Strouhal number of 0.08, near the maximum absorption. The agreement is less good for Strouhal numbers away from maximum absorption, where the analytical model overpredicts the absorption, as is seen in Fig. 5. This is thought to be a result of using an infinitessimally thin shear layer for the shed vorticity in the analytical model, which is likely to respond to acoustic forcing over a broader range of Strouhal numbers than a real shear layer with a finite thickness. To test this, we performed the same calculation for the same geometry and Mach number, but different displacement thickness. Results are shown in Fig. 6, where + is for a displacement thickness of 3.5 mm and ○ is for a displacement thickness of 4.5 mm. Note that the thinner boundary layer does indeed give absorption over a broader range of Strouhal numbers. In conclusion, there is a great advantage in using compact Green's functions because then accurate predictions for the sound field can be obtained, even with low-order numerical schemes.

VI. Effects of Pipe Resonances

In any real pipework system the pipes will be of finite length. Reflection from the ends of these pipes will result in sound waves incident on the expansion both from the left and from the right. This is illustrated in Fig. 7. An incident sound wave B_0 propagates from left to right toward the backward-facing step at $y_1 = 0$. This incident

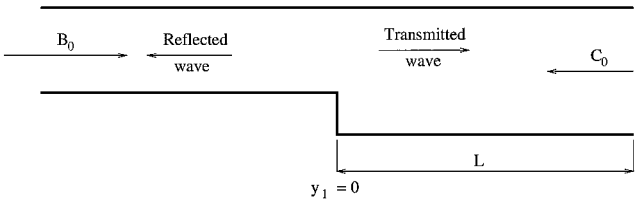

Fig. 7 Finite-length pipe geometry.

wave is partly reflected and partly transmitted into the larger section of the pipework channel (where $y_1 > 0$). The transmitted wave propagates from left to right toward the end of the pipework system at $y_1 = L$. There it is reflected back toward the expansion forming a second incident sound wave C_0. Just as for the infinite pipe problem, there is a mean flow passing through the system from left to right. Provided $kH < \pi$ and kL is large, the reflected wave C_0 will be planar and so entirely equivalent to an incident wave propagating from $y_1 = +\infty$. The effect of this second incident wave might be included into the computational calculation by replacing the nonreflecting boundary condition downstream with a reflecting boundary condition on $y_1 = L$. Alternatively, because we wish to concentrate our computational resources into the nonlinear flow region and we can calculate the acoustic waves, we might take the computation boundary upstream of $y_1 = L$. Then we need to include an analytical description of the reflection of waves from a specific length channel. This will, of course, be related to the outgoing wave at an earlier time. Alternatively, we can use a consequence that is evident in the analytical model.

The effects of the finite length channels become fully evident through the analytical model. An incoming wave from $y_1 \to +\infty$ is represented, in the ζ plane as a sink at $\zeta = 0$. This second incident sound wave then also sheds vorticity at the lip of the expansion but of opposite phase to the wave incident from $y_1 \to -\infty$. Hence the vorticity strength is proportional to the vorticity strength already found for the infinite pipe system, the coefficient of proportionality being $(B_0 - C_0)/B_0$. The significance of this is that the radiated sound field for any length pipes is easily derived from the solution for the infinite pipes. This fact can be used to calculate the sound field from the computational calculation for the infinite pipes without performing a second calculation.

The absorption coefficient definition must now be altered to account for the second incident sound wave. Thus we have

$$\Delta_L = \frac{I_{1\text{in}}A_1 + I_{2\text{in}}A_2 - I_{1\text{out}}A_1 - I_{2\text{out}}A_2}{I_{1\text{in}}A_1 + I_{2\text{in}}A_2} \tag{54}$$

where

$$I_{1\text{in}} = \frac{p'^2_{1\text{in}}}{\rho c}(1 + M_1)^2 = \frac{B'^2_{1\text{in}}}{c} \tag{55}$$

$$I_{2\text{in}} = \frac{p'^2_{2\text{in}}}{\rho c}(1 - M_2)^2 = \frac{B'^2_{2\text{in}}}{c} \tag{56}$$

$$I_{1\text{out}} = \frac{p'^2_{1\text{out}}}{\rho c}(1 - M_1)^2 = \frac{B'^2_{1\text{out}}}{c} \tag{57}$$

$$I_{2\text{out}} = \frac{p'^2_{2\text{out}}}{\rho c}(1 + M_2)^2 = \frac{B'^2_{2\text{out}}}{c} \tag{58}$$

We now compare the predicted absorption coefficients with experimental measurements.

VII. Comparison with Experiment

The arrangement for the experimental setup is illustrated in Fig. 8. This is not drawn to scale. Ambient air enters a rectangular channel of length 0.5 m, height 0.05 m, and width 0.05 m, through a smooth bellmouth. There is an abrupt area change into a second channel of length 1 m, height 0.067 m, and width 0.05 m, forming a backward-facing step as illustrated in Fig. 8. The two channels are connected in such a way that the only change between the two is a sudden change in height. The second channel is connected to an axial blower that induces the steady flow. The mean flow is measured at the inlet, 0.02 m downstream of the bellmouth, using a hot wire to an accuracy of 3%.

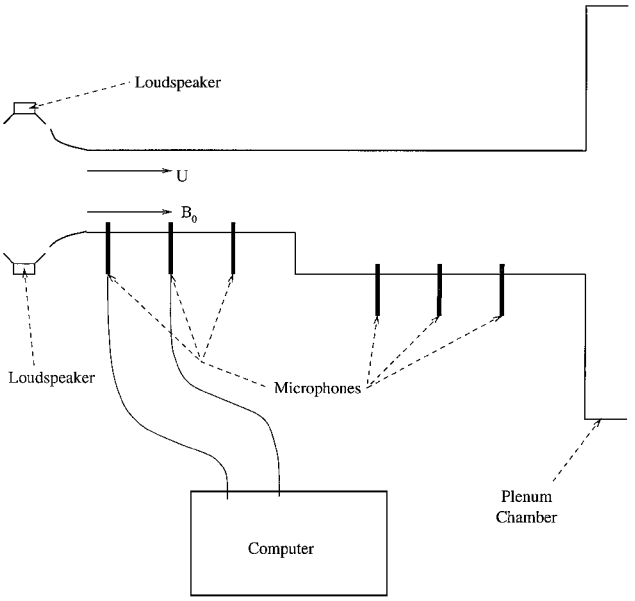

Fig. 8 Experimental setup for the two-dimensional channels.

The displacement thickness at the step is found to be approximately 3.5 mm. The analytical model in Eq. (31) requires that the mean flow boundary layer is much thicker than the acoustic shear layer, i.e., much greater than the Stokes layer $(2\nu/\omega)^{1/2}$. For the lowest frequency of interest in the experiment, 70 Hz, this gives an estimated acoustic shear layer thickness of 0.2 mm. Thus the thickness of the mean shear layer is larger than the acoustic shear layer by at least a factor of 20.

The representation theory described in Sec. II requires a low Mach number so that terms of order M^2 may be neglected. Here, as in the computation, we use a Mach number of 0.25, which is close to the maximum Mach number we could use and still make this approximation.

Acoustic waves are generated by an arrangement of four loudspeakers at the inlet of the pipe system, as shown in Fig. 8. This loudspeaker system is excited at a single frequency providing an incident sound wave that propagates through the pipework system from left to right toward the expansion. The frequency range is from 70 to 300 Hz. The largest frequency (300 Hz) corresponds to a Helmholtz number (based on the large pipe height) kH of 0.362 ($\ll\pi$). Hence the higher-order modes, for which $n \geq 1$, decay very rapidly (the $n = 1$ mode decays by 20 dB within 42 mm in the larger pipe and within 36 mm in the smaller pipe).

The pressure waves in both pipes are measured by three microphones in each pipe. The six microphones are connected to a computer (as illustrated in Fig. 8) that calculates the auto- and cross-spectral densities of the pressures measured by the microphones. Seybert and Ross[23] show that the left and right propagating acoustic waves can be related to these spectral densities. The microphones are calibrated as suggested by Seybert and Ross.[23] Using three microphones in each pipe serves as a check that only plane waves are propagating because each pair of microphones in a given pipe should yield the same forward and reverse propagating waves. The phase between the waves in each pipe is calculated by taking readings with one microphone in each pipe. At each frequency checks were made that the readings varied linearly with incident wave amplitude. When this was not the case, the incident wave magnitude was reduced to move the readings into the linear regime.

The spacing of the microphones in each pipe requires careful thought. Seybert and Soenarko[24] show that the spacing should be kept small, in particular $kd < \pi$, where d is the microphone spacing, to achieve high coherence. The microphone spacing must not be too small, however, otherwise the readings taken from them will be effectively of the same pressures for low frequency, for which the wavelength is large. A compromise of 0.1 m is therefore taken. The microphones are also placed sufficiently far from the ends of

the pipes that only plane waves are propagating. Here they are a distance 0.2 m from the end of the first pipe (so the first mode has decayed by at least 125 dB) and a distance 0.3 m from the end of the second pipe (so the first mode has decayed by at least 138 dB) at the nearest microphone.

The ratio of the left- and right-traveling sound waves is measured in the larger pipe, and thus the reflection coefficient from the duct exit at $y_1 = L$, R_L, is determined. This can then be used in the calculation to convert the semi-infinite pipe calculations to finite-length pipe calculations:

$$C_0(\omega) = R_L T_f B_0 = R_L(T_{\text{il}} B_0 + R_{\text{ir}} C_0) \tag{59}$$

$$\Rightarrow T_f(\omega) = \frac{T_{\text{il}}}{1 - R_L R_{\text{ir}}} \tag{60}$$

$$R_f(\omega) = R_{\text{il}} + T_{\text{ir}}(C_0/B_0) \tag{61}$$

$$\Rightarrow R_f(\omega) = \frac{R_{\text{il}}(1 - R_L R_{\text{ir}}) + T_{\text{il}} T_{\text{ir}} R_L}{1 - R_L R_{\text{ir}}} \tag{62}$$

$$C_0(\omega) = R_L \left(\frac{T_{\text{il}}}{1 - R_L R_{\text{ir}}}\right) B_0 \tag{63}$$

where T_{il} and R_{il} are the stagnation enthalpy transmission and reflection coefficients, respectively, for an incident wave traveling from left to right from $y_1 = -\infty$ in semi-infinite channels; T_{ir} and R_{ir} are the stagnation enthalpy transmission and reflection coefficients for an incident wave traveling from right to left from $y_1 = \infty$ in semi-infinite channels; and $T_f(\omega)$ and $R_f(\omega)$ are the stagnation enthalpy transmission and reflection coefficients for finite-length channels. For these relations to hold R_L, the stagnation enthalpy reflection coefficient for the end of the channel must be expressed in terms of sound waves at $y_1 = 0$.

Figure 9 shows the comparison between the numerical (○), analytical (−), and experimental (+) results for the absorption coefficient Δ_L in finite-length pipes with a mean flow Mach number of 0.25. Only the computational calculations made using the compact Green's functions are shown.

The graph for the absorption coefficient has three maxima at three different Strouhal numbers. Because absorption in infinite channels occurs over a fairly wide range of Strouhal numbers, all three maxima correspond to enhancement of the absorption process by half wavelength resonances in the second pipe. Note that all three represent significant absorption (55–65%, 65–80%, and 35–45%, respectively). Thus resonance in the second pipe can significantly enhance the absorption. Note also that the second, at a Strouhal number based upon step height of 0.052, gives a larger absorption coefficient than the other two. The probable reason for this is that the natural absorption in infinite pipes is larger at this Strouhal number. At frequencies corresponding to odd multiples of one-quarter wavelengths in the small pipe (Strouhal numbers of 0.0135, 0.0405, 0.0675, and 0.0945), the absorption drops to zero and then goes negative, as seen in Fig. 9. Zero absorption occurs when C_0 equals B_0, and so no vorticity is shed from the lip. At these Strouhal numbers the linear effect of vortex shedding is small, and so nonlinear effects dominate. Although checks were carried out to reduce this, the scatter in the readings may be partly a result of this. Moreover, the lower amplitude of the incident wave allows other effects, such as the turbulence, to have a proportionally larger effect.

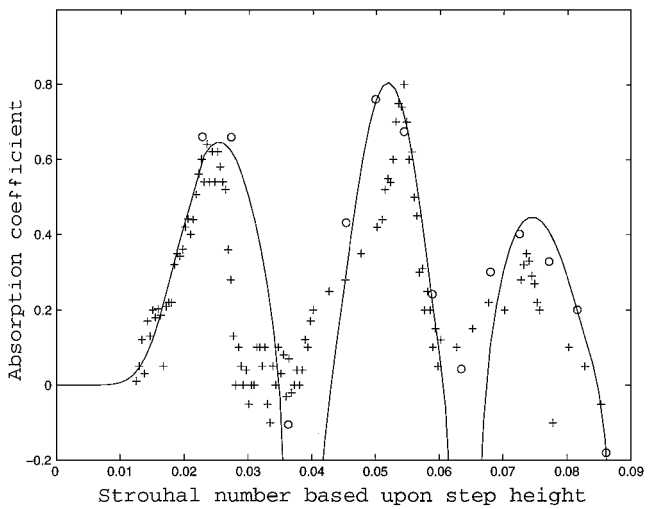

Fig. 9 Comparison between the calculated and measured absorption coefficients for finite-length pipes at $M = 0.25, H/h = 1.35, L/h = 50$: ——, analytical calculation; ○, numerical calculation; and +, experimental results.

The agreement between the experimental data and the two calculations is very encouraging. The Strouhal numbers corresponding to the three maxima agree to within 4%. The magnitude of absorption coefficient at the maxima also agree to within 5% for the first two maxima, with both the computation and the analytical calculation data points falling within the experimental data points, suggesting that the predictions are within experimental errors. At a Strouhal number of 0.078, the agreement is less good, but still within 10%. The analytical solution does, however, predict broader peaks just as it did in the calculation for semi-infinite ducts in Fig. 5.

VIII. Conclusions

In this paper we have discussed the use of the compact Green's function in calculating the sound absorbed when an incident sound wave propagates past a sudden area expansion in a two-dimensional channel in the presence of a mean flow. In particular we note that this Green function emphasizes the effect of sources near the lip of the expansion on the radiated far-field sound. As a result, the description of the main acoustic source, the vorticity field, can be relatively crude provided it is accurate near the lip of the expansion. Indeed, good agreement is found with the experiment even though a very crude turbulence model was used. We have also investigated the use of two other Green's functions based on the modes of straight-walled semi-infinite pipes. These can also be used in a formally exact acoustic analogy, but one that now involves additional surface terms at the expansion. However, we find these formulations to be more prone to errors in the source terms, and recommend the use of a compact Green's function. Our infinite pipe predictions suggest that a backward-facing step is a modest absorber of sound, with a maximum absorption coefficient of about 0.3 over a broad range of Strouhal numbers (based upon step height) of between about 0.03 and 0.1, with a maximum absorption at a Strouhal number of about 0.07. We have extended the analysis to include the effect of pipe resonances, noting that very high absorption is found near half-wavelength resonances. Both the numerical and the analytical calculation using the compact Green's function give reasonable agreement with the experiment except near one-quarter wavelength resonances, where the theoretical absorption drops to zero and so the nonlinear effects become more important in the experiment.

Appendix: Derivation of the Compact Green's Function

We wish to determine an approximate solution to Eq. (23), subject to the boundary conditions (24) and (25). To eliminate the steady potential flow velocity $\boldsymbol{U}$ from Eq. (23), we follow the approach of Howe[17] and rewrite G in new variables $\boldsymbol{Y}$, $\boldsymbol{X}$, τ', and t' defined by Taylor's transformation (see Ref. 25):

$$\boldsymbol{Y} = \boldsymbol{y}, \qquad \tau' = \tau + \bar{\phi}(\boldsymbol{y})/c^2 \tag{A1}$$

$$\boldsymbol{X} = \boldsymbol{x}, \qquad t' = t + \bar{\phi}(\boldsymbol{x})/c^2 \tag{A2}$$

$$G'(\boldsymbol{X}, t' \mid \boldsymbol{Y}, \tau') = G(\boldsymbol{x}, t \mid \boldsymbol{y}, \tau) \tag{A3}$$

where $\bar{\phi}(\boldsymbol{y})$ is the potential for the hypothetical velocity field $\boldsymbol{U}$. It is again convenient to work in the frequency domain, and so we write

$$G'(\boldsymbol{X}, t' \mid \boldsymbol{Y}, \tau') = \frac{1}{2\pi} \int_{\omega} \hat{G}(\boldsymbol{X}, t' \mid \boldsymbol{Y}, \omega) \exp(i\omega\tau')\, \mathrm{d}\omega$$

$\hat{G} \exp(i\omega\tau')$ is the response to a harmonic source of angular frequency ω. We will calculate $\hat{G}_c$, the low-frequency form of $\hat{G}$ (i.e., $kH < \pi$).

k|X₁| ≫ 1, |Y₁| ≫ h

We initially restrict our attention to cases when both the observer's position is far from the step, i.e., $k|X_1| \gg 1$, and when $\boldsymbol{Y}$ is away from $\boldsymbol{X}$ and the junction, i.e., $|\boldsymbol{X}-\boldsymbol{Y}| \gg h$, $|Y_1| \gg h$. Then the Green's function consists of plane waves, and its determination is straightforward.

For $kX_1 \ll -1$:

$$\hat{G}_c \exp(i\omega\tau') = A\exp[i\omega(\tau' - t')]\{\exp(ik|X_1 - Y_1|) + R_1\exp[-ik(X_1 + Y_1)]\} \qquad Y_1 \ll 0 \quad \text{(A4)}$$

$$= AT_1\exp[i\omega(\tau' - t')]\exp[-ik(X_1 - Y_1)] \qquad 0 \ll Y_1 \quad \text{(A5)}$$

and for $kX_1 \gg 1$:

$$\hat{G}_c \exp(i\omega\tau') = B\exp[i\omega(\tau' - t')]\{\exp(-ik|X_1 - Y_1|) + R_2\exp[ik(X_1 + Y_1)]\} \qquad 0 \ll Y_1 \quad \text{(A6)}$$

$$= BT_2\exp[i\omega(\tau' - t')]\exp[ik(X_1 - Y_1)] \qquad Y_1 \ll 0 \quad \text{(A7)}$$

where R_1 and T_1 are the plane wave stagnation enthalpy reflection and transmission coefficients for an incident wave from $X_1 \ll 0$, respectively, whereas R_2 and T_2 are the corresponding reflection and transmission coefficients for an incident wave from $X_1 \gg 0$. In the preceding expressions the comparison is with the channel height and not the wavelength, and so $X_1 \ll Y_1$ means that $Y_1 - X_1$ is large in comparison with H and not necessarily in comparison with c/ω.

R_1, R_2, T_1, T_2 in the transformed variables $\boldsymbol{X}$, $\boldsymbol{Y}$, t', and τ' are as for the normal case of plane waves transmitted across an area change[26]:

$$R_1 = (h-H)/(h+H), \qquad T_1 = 2h/(h+H)$$
$$R_2 = (H-h)/(h+H), \qquad T_2 = 2H/(h+H) \quad \text{(A8)}$$

The constants A and B in Eqs. (A4–A7) can be determined by integration of Eq. (23) across the singularity, which leads to[18] $A = -1/2ikh$ and $B = -1/2ikH$.

When rewritten in terms of $\boldsymbol{x}$, $\boldsymbol{y}$, t, and τ, these equations give

$$\hat{G}_c \exp(i\omega\tau) = \frac{-1}{2ikh}\exp[i\omega(\tau - t)]\exp[ikM_1(y_1 - x_1)] \times \left\{\exp(ik|y_1 - x_1|) + \frac{h-H}{H+h}\exp[-ik(y_1 + x_1)]\right\} \qquad x_1, y_1 \ll 0 \quad \text{(A9)}$$

$$= \frac{-1}{2ikH}\exp[i\omega(\tau - t)]\exp[ikM_2(y_1 - x_1)] \times \left\{\exp(-ik|y_1 - x_1|) + \frac{H-h}{H+h}\exp[ik(y_1 + x_1)]\right\} \qquad 0 \ll x_1, y_1 \quad \text{(A10)}$$

$$= \frac{-1}{ik(H+h)}\exp[i\omega(\tau - t)]\exp\left(\frac{-ikx_1}{1-M_1}\right)\exp\left(\frac{iky_1}{1-M_2}\right) \qquad x_1 \ll 0 \ll y_1 \quad \text{(A11)}$$

$$= \frac{-1}{ik(H+h)}\exp[i\omega(\tau - t)]\exp\left(\frac{ikx_1}{1+M_2}\right)\exp\left(\frac{-iky_1}{1+M_1}\right) \qquad y_1 \ll 0 \ll x_1 \quad \text{(A12)}$$

***k|X₁| ≫ 1, Y* in Near Field**

Near the junction $k|Y_1| \ll 1$, the wave equation reduces to the incompressible form $\nabla^2\hat{G}_c = 0$ with $\partial\hat{G}_c/\partial n = 0$ on all rigid walls. Thus if $\Phi(\boldsymbol{Y})$ is the potential flow solution for flow past a backward-facing step that asymptotes to the same solution as the outer form shown for $k|Y_1| \ll 1$, but $|Y_1| \gg H$ (Ref. 27), i.e.,

$$\Phi \to (H/h)Y_1 \quad \text{as} \quad Y_1 \to -\infty$$
$$\Phi \to Y_1 \quad \text{as} \quad Y_1 \to +\infty \quad \text{(A13)}$$

then in the region $k|Y_1| \ll 1$, $\hat{G}_c$ takes the form

$$\hat{G}_c \exp(i\omega\tau') = -\frac{\exp[i\omega(\tau' - t') - kX_1]}{ik(H+h)}[1 + ik\Phi(\boldsymbol{Y})] \qquad X_1 \ll 0 \quad \text{(A14)}$$

$$= \frac{\exp[i\omega(\tau' - t') + kX_1]}{ik(H+h)}\left[ik\frac{h}{H}\Phi(\boldsymbol{Y}) - 1\right] \qquad 0 \ll X_1 \quad \text{(A15)}$$

Finally, rewriting in terms of $\boldsymbol{x}$, $\boldsymbol{y}$, t, τ,

$$\hat{G}_c \exp(i\omega\tau) = -\frac{\exp\{i\omega[\tau - t - x_1/c(1-M_1)]\}}{ik(H+h)} \times [1 + ik\Phi(\boldsymbol{y})] \qquad x_1 \ll 0 \quad \text{(A16)}$$

$$= -\frac{\exp\{i\omega[\tau - t + x_1/c(1+M_2)]\}}{ik(H+h)} \times \left[1 - ik\frac{h}{H}\Phi(\boldsymbol{y})\right] \qquad 0 \ll x_1 \quad \text{(A17)}$$

correct to order M^2. Φ is given by Eq. (28). The compact Green's function for x_1 in the far field and $\boldsymbol{y}$ in the near field is given by substitution for Φ from Eq. (28) into Eqs. (A14–A17):

$$\hat{G}_c \exp(i\omega\tau) = -\frac{\exp\{i\omega[\tau - t - x_1/c(1-M_1)]\}}{ik(H+h)} \times \left(1 + ik\frac{H}{\pi}\ell n\zeta\right) \qquad x_1 \ll 0 \quad \text{(A18)}$$

$$= -\frac{\exp\{i\omega[\tau - t + x_1/c(1+M_2)]\}}{ik(H+h)} \times \left(1 - ik\frac{hH}{\pi}\ell n\zeta\right) \qquad 0 \ll x_1 \quad \text{(A19)}$$

***X* and *Y* in the Near Field**

To obtain the form of G_c for $\boldsymbol{X}$ in the near field, we need to know the G_c field at $\boldsymbol{Y}$ caused by a sink at $\boldsymbol{X}$. When both $\mathbf{Y}$ and $\boldsymbol{X}$ are in the near field, this is essentially the solution to the incompressible problem $\partial^2 G_c/\partial Y_i \partial Y_i = \delta(\boldsymbol{X} - \boldsymbol{Y})$. The coefficients can be obtained by matching the form of this for $|Y_1|/H \to \pm\infty$ (but $k|Y_1| \ll 1$) to inward propagating waves. Figure 2 depicts the inner flow region in which $|X_1|$ and $|Y_1|$ are both small. The distance L, shown, is assumed to be small in comparison with the wavelength but large in comparison with H. On the edge of this region, the Y_1 dependence is taken to be $C\exp[j\omega(\tau' - t')](1 - j\omega Y_1/c)$ for $Y_1 \ll 0$ and to be $D\exp[j\omega(\tau' - t')](1 + j\omega Y_1/c)$ for $Y_1 \gg 0$. Here j represents $\sqrt{-1}$ and is used to distinguish it from i used in the conformal transformation. In the inner flowfield G_c satisfies Laplace's equation and takes the form

$$\hat{G}_c(\zeta \mid \zeta_x)\exp(j\omega\tau') = \Re\left[\frac{\ell n(\zeta - \zeta_x)}{2\pi} - \frac{\ell n(\zeta - \zeta_x^*)}{2\pi} + \mu\frac{\ell n\zeta}{2\pi} + E\right]\exp[j\omega(\tau' - t')] \quad \text{(A20)}$$

We can now find C, D, μ, and E by matching at $Y_1 \to -\infty$ and $Y_1 \to \infty$, noting that $\ln\zeta \to \pi z/h$ as $Y_1 \to -\infty$ and $\ln\zeta \to \pi z/H$ as $Y_1 \to \infty$. The result is

$$C = -\frac{1}{jk(H+h)} - \left(\frac{H}{H+h}\right)\frac{\ln|\zeta_x|^2}{2\pi}$$

$$D = \left(\frac{h}{H+h}\right)\frac{\ln|\zeta_x|^2}{2\pi} - \frac{1}{jk(H+h)} \tag{A21}$$

$$E = \left(\frac{h}{H+h}\right)\frac{\ln|\zeta_x|^2}{2\pi} - \frac{1}{jk(H+h)}$$

$$\mu = \frac{2h}{H+h} + jkH\left(\frac{h}{H+h}\right)\frac{\ln|\zeta_x|^2}{\pi} \tag{A22}$$

The form of G_c for $\boldsymbol{X}$ in the near field and $\boldsymbol{Y}$ in the far field can be obtained from Eq. (A21). When rewritten in terms of $\boldsymbol{x}, t, \boldsymbol{y}, \tau$, it is

$$\hat{G}_c \exp(i\omega\tau) = \frac{-1}{ik(H+h)} \exp[i\omega(\tau - t)]$$

$$\times \exp\left[\frac{-iky_1}{c(1-M_1)}\right]\left(1 + ik\frac{H}{\pi}\ln\zeta_x\right) \qquad Y_1 \ll 0 \tag{A23}$$

$$\hat{G}_c \exp(i\omega\tau) = \frac{-1}{ik(H+h)} \exp[i\omega(\tau - t)]$$

$$\times \exp\left[\frac{+iky_1}{c(1+M_2)}\right]\left(1 - ik\frac{h}{\pi}\ln\zeta_x\right) \qquad 0 \ll Y_1 \tag{A24}$$

Finally, we note that the asymptotic forms for $\hat{G}_c$ from Eqs. (A20) and (A22) for $c/\omega \gg |Y_1|, |X_1| \gg H$ match those obtained from Eqs. (A18), (A19), (A11), and (A12).

Acknowledgments

This work was mostly carried out while I. D. J. Dupère was in receipt of an Engineering and Physical Sciences Research Council scholarship, whose support is gratefully acknowledged. The authors are indebted to J. D. Denton for making his code VISQ3D available.

References

[1]Bechert, D., "Sound Sinks in Flows. A Real Possibility?" edited by E.-A. Muller, *Mechanics of Sound Generation in Flows*, Springer–Verlag, London, 1979, pp. 26–34.

[2]Bechert, D. W., "Sound Absorption Caused by Vorticity Shedding, Demonstrated with a Jet Flow," *Journal of Sound and Vibration*, Vol. 70, No. 3, 1980, pp. 389–405.

[3]Hourigan, K., Welsh, M. C., Thompson, M. C., and Stokes, A. N., "Aerodynamic Sources of Acoustic Resonance in a Duct with Baffles," *Journal of Fluids and Structures*, Vol. 4, No. 4, 1990, pp. 345–370.

[4]Howe, M. S., "On the Absorption of Sound by Turbulence and Other Hydrodynamic Flows," *Journal of Applied Mathematics*, Vol. 32, No. 1–3, 1984, pp. 187–209.

[5]Howe, M. S., "Attenuation of Sound Due to Vortex Shedding from a Splitter Plate in a Mean Flow Duct," *Journal of Sound and Vibration*, Vol. 105, No. 3, 1986, pp. 385–396.

[6]Peters, M. C. A. M., Hirschberg, A., Rijnen, A. J., and Wijnands, A. P. J., "Damping and Reflection Measurements for an Open Pipe at Low Mach and Low Helmholtz Numbers," *Journal of Fluid Mechanics*, Vol. 256, 1993, pp. 499–534.

[7]Peters, M. C. A. M., and Hirschberg, A., "Acoustically Induced Periodic Vortex Shedding at Sharp Edged Open Channel Ends: Simple Vortex Models," *Journal of Sound and Vibration*, Vol. 161, No. 2, 1993, pp. 281–299.

[8]Wendoloski, J. C., "Sound Absorption by an Orifice Plate in a Flow Duct," *Journal of the Acoustical Society of America*, Vol. 104, No. 1, 1998, pp. 122–132.

[9]Borth, W., "Vibration and Resonance Phenomena in the Ducts of Piston Compressors," *Zeitschrift des Vereins Deutsches Ingenieure*, Vol. 60, No. 28, 1916, pp. 565–569.

[10]Ingard, U. V., and Labate, S., "Acoustic Circulation Effects and Nonlinear Impedance of Orifices," *Journal of the Acoustical Society of America*, Vol. 22, No. 2, 1950, pp. 211–218.

[11]Ingard, U. V., and Ising, H., "Acoustic Nonlinearity of an Orifice," *Journal of the Acoustical Society of America*, Vol. 42, No. 1, 1967, pp. 6–17.

[12]Cummings, A., "Acoustic Nonlinearities and Power Losses at Orifices," *AIAA Journal*, Vol. 22, No. 6, 1984, pp. 786–792.

[13]Cummings, A., "Transient and Multiple Frequency Sound Transmission Through Perforated Plates at High Amplitude," AIAA Paper 84-2311, Oct. 1984.

[14]Howe, M. S., "On the Theory of Unsteady High Reynolds Number Flow Through a Circular Aperture," *Proceedings of the Royal Society of London*, Vol. A366, No. 1725, 1979, pp. 205–223.

[15]Hughes, I. J., and Dowling, A. P., "The Absorption of Sound by Perforated Linings," *Journal of Fluid Mechanics*, Vol. 218, 1990, pp. 299–335.

[16]Howe, M. S., "On the Diffraction of Sound by a Screen with Circular Apertures in the Presence of a Low Mach Number Grazing Flow," *Proceedings of the Royal Society of London*, Vol. A370, No. 1743, 1980, pp. 523–544.

[17]Howe, M. S., "Attenuation of Sound in a Low Mach Number Nozzle Flow," *Journal of Fluid Mechanics*, Vol. 91, 1979, pp. 625–673.

[18]Dupère, I. D. J., "Sound Vortex Interaction in Pipes," Ph.D. Dissertation, Dept. of Engineering, Univ. of Cambridge, Cambridge, England, U.K., June 1997.

[19]Currie, I. G., *Fundamentals Mechanics of Fluids*, 2nd ed., McGraw–Hill, New York, 1993, pp. 115–118.

[20]Lighthill, M. J., *Waves in Fluids*, Cambridge Univ. Press, Cambridge, England, U.K., 1978, pp. 130–136.

[21]Denton, J. D., "An Improved Time-Marching Method for Turbomachinery Flow Calculation," *Journal of Engineering for Power*, Vol. 105, No. 3, 1983, pp. 514–524.

[22]Morfey, C. L., "Sound Transmission and Generation in Ducts with Flow," *Journal of Sound and Vibration*, Vol. 14, No. 1, 1971, pp. 37–55.

[23]Seybert, A. F., and Ross, D. F., "Experimental Determination of Acoustic Properties Using a Two Microphone Random Excitation Technique," *Journal of the Acoustical Society of America*, Vol. 61, No. 5, 1977, pp. 1362–1370.

[24]Seybert, A. F., and Soenarko, B., "Error Analysis of Spectral Estimates with Application to the Measurement of Acoustic Parameters Using Random Sound Fields in Ducts," *Journal of the Acoustical Society of America*, Vol. 69, No. 4, 1981, pp. 1190–1199.

[25]Crighton, D. G., Dowling, A. P., Ffowcs Williams, J. E., Heckl, M., and Leppington, F. G., *Modern Methods in Analytical Acoustics*, Springer–Verlag, London, 1992, p. 415.

[26]Dowling, A. P., and Ffowcs Williams, J. E., *Sound and Sources of Sound*, Ellis Horwood, Chichester, England, U.K., 1983, p. 64.

[27]Howe, M. S., *Acoustics of Fluid-Structure Interactions*, Cambridge Univ. Press, Cambridge, England, U.K., 1998, pp. 167–186.

M. Samimy
Associate Editor